University of Groningen

Binding of azobenzene and p-diaminoazobenzene to the human voltage-gated sodium channel Nav1.4

Palmisano, Vito F.; Gómez-Rodellar, Carlos; Pollak, Hannah; Cárdenas, Gustavo; Corry, Ben; Faraji, Shirin; Nogueira, Juan J.

IMPORTANT NOTE: You are advised to consult the publisher's version (publisher's PDF) if you wish to cite from it. Please check the document version below.

Document Version
Publisher's PDF, also known as Version of record

Publication date:
2021

[Link to publication in University of Groningen/UMCG research database](#)

Binding of azobenzene and *p*-diaminoazobenzene to the human voltage-gated sodium channel Na$_v$1.4

Vito F. Palmisano,[ab] Carlos Gómez-Rodellar,[a] Hannah Pollak,[a] Gustavo Cárdenas,[a] Ben Corry, ID *[c] Shirin Faraji ID *[b] and Juan J. Nogueira ID *[ad]

The activity of voltage-gated ion channels can be controlled by the binding of photoswitches inside their internal cavity and subsequent light irradiation. We investigated the binding of azobenzene and p-diaminoazobenzene to the human Na$_v$1.4 channel in the inactivated state by means of Gaussian accelerated molecular dynamics simulations and free-energy computations. Three stable binding pockets were identified for each of the two photoswitches. In all the cases, the binding is controlled by the balance between the favorable hydrophobic interactions of the ligands with the nonpolar residues of the protein and the unfavorable polar solvation energy. In addition, electrostatic interactions between the ligand and the polar aminoacids are also relevant for p-diaminoazobenzene due to the presence of the amino groups on the benzene moieties. These groups participate in hydrogen bonding in the most favorable binding pocket and in long-range electrostatic interactions in the other pockets. The thermodinamically preferred binding sites found for both photoswitches are close to the selectivity filter of the channel. Therefore, it is very likely that the binding of these ligands will induce alterations in the ion conduction through the channel.

1 Introduction

The use of effective and safe pharmacotherapies to treat both acute and chronic medical disorders has contributed to improve the quality of life of our society.[1] However, drug-related issues are still present in many therapies, including poor drug selectivity, which leads to undesired interactions of the drug with biomolecules other than the planned target.[2,3] Low drug selectivity is related to several drawbacks, including short and long-term side effects in patients, the use of sub-optimal dosage, and adverse environmental impact due to the released activity from drugs even when they are outside of the organism.[4] To tackle the problems related to selectivity and toxicity, light has been recently thought as a solution due to its capacity to have high temporal resolution over the drug activity and non-invasive spatial precision.[5] Light shows a large degree of orthogonality towards most biochemical systems, since

photons with wavelength within the therapeutic window do not contaminate the systems and have low toxicity. In addition, light can be regulated by adjusting the wavelength and intensity to ensure a safe and controlled usage.[6] Photopharmacology – or optopharmacology – has been developed in the last decades to design chemical compounds, named photoswitches, which undergo reversible changes in their structure and properties upon absorption of light and are able to control the functions of biological molecules.[2,4,7,8]

Azobenzene (AZ) has been the most widely employed photoswitch for biological environments.[5,6,9,10] The *trans* conformation of AZ is the dominant isomer in the dark (in the electronic ground state) at equilibrium. However, the *cis* isomer can be easily populated by irradiation with UV light. The photoisomerization of AZ has been intensively investigated by means of theoretical methods and spectroscopic measurements, and several mechanisms have been proposed.[11] Although some contradictions have been found in different studies, it is generally agreed that isomerization occurs *via* the S$_1$ state, which has n → π* character and is mainly dark. In addition, the photoisomerization occurs with the highest quantum yield following direct excitation to the S$_1$ state, while population of this state by internal conversion from the bright S$_2$ state of π → π* character results in a lower quantum yield.[11] The S$_1$ state prepared by S$_2$/S$_1$ internal conversion has an excess of

[a] *Department of Chemistry, Universidad Autónoma de Madrid, Calle Francisco Tomás y Valiente, 7, 28049, Madrid, Spain. E-mail: juan.nogueira@uam.es*

[b] *Theoretical Chemistry Group, Zernike Institute for Advanced Materials, University of Groningen, Groningen, The Netherlands. E-mail: s.s.faraji@rug.nl*

[c] *Research School of Biology, Australian National University, Acton, Canberra, Australia. E-mail: ben.corry@anu.edu.au*

[d] *IADCHEM, Institute for Advanced Research in Chemistry, Universidad Autónoma de Madrid, Calle Francisco Tomás y Valiente, 7, 28049 Madrid, Spain*

vibrational energy that opens additional deactivation pathways, decreasing the *trans → cis* photoisomerization quantum yield. This vibrational excitation can be reduced by decreasing the energy gap between the S_2 and S_1 electronic states. For example, functionalization of AZ with electron-donating substituents, *e.g.*, amino groups, induces a red shift of the S_2 state, leading to an overlap with the S_1 state.[12,13] As a consequence, the photoisomerization yield is found to be higher for amino derivatives of AZ than for AZ itself. In addition, the red shift of the bright state upon functionalization can make the photoswitches suitable for their use in *in vivo* systems. The absorption of radiation within the UV range by AZ and some of its derivatives can induce harmful effects in cells and is appropriate only for *in vitro* applications.[6]

In the last years, several photoswitches have been designed to modulate the activity of voltage-gated ion channels.[14,15] These transmembrane proteins play a central role in human physiology since they are responsible for the generation and propagation of action potentials in neurons and other excitable cells.[16] This underlies a wide range of biological processes, such as the transmission of nerve impulses and stimulation of muscle contraction. Moreover, the abnormal function of those channels due to genetic mutations are associated with a wide range of diseases, called channelopathies.[17,18] Therefore, voltage-gated ion channels are ideal targets for drug discovery. Since action potentials are generated by the movement of ions across cell membranes through the ion channels,[19] the regulation of ion permeation by the combined action of light and a photoswitch is a potential tool to manipulate the function of voltage-gated ion channels with high spatiotemporal precision. In the last decade, AZ derivatives have been employed to alter the activity of several channels.[15,20–23] For example, it was found that a diquaternary ammonium AZ (QAQ) photoswitch was able to block ion conduction through voltage-gated Na^+, K^+ and Ca^{2+} channels in the *trans* form but not in the *cis* form. *In vivo* assays in rats have shown that QAQ enables reversible optical silencing of mouse nociceptive neurons, serving as a light-sensitive analgesic.[20]

The first step of this intricate photoinduced mechanism that aims to block ion conduction is the binding of the most stable conformation of the photoswitch at equilibrium in the ground state to the voltage-gated ion channel. Previous docking simulations of QAQ interacting with a chimeric Kv1.2–2.1 K^+ channel have shown that both the *trans* and *cis* isomers of the photoswitch are located in the central cavity of the channel, close to the selectivity filter, although with different orientations.[23] Specifically, the positively charged quaternary ammonium moiety of the photoswitch is directly below the selectivity filter of the channel for the *trans* isomer, while it moves away from the filter for the *cis* isomer. The predicted position of the quaternary ammonia in the *trans* isomer is similar to that previously seen for crystal structures of quaternary ammonium blockers co-crystallized with the prokaryotic K^+ channel KcsA.[24,25] Despite these previous structural studies, little is known about the mechanism that drives the binding process of photoswitches to ion channels, especially in Na^+ channels. In

this work, we search the binding pockets of two photoswitches in the *trans* conformation, namely AZ and *p*-diamonoazobenzene (*p*-DAZ), into the central cavity of the human voltage-gated Na^+ channel $Na_v1.4$,[26] which was structurally resolved in an inactivated state, by means of Gaussian accelerated molecular dynamics (GaMD).[27] Although the ability of these two photoswitches to block the ion conduction through ion channels have not been experimentally addressed, their simple chemical structure makes them ideal models to be used in theoretical simulations to gain insight into the binding process mechanism. Specifically, the relevance of the different protein amino acids in each of the pockets is discussed in terms of their contribution to the estimated binding free energy, and an energy-decomposition analysis enables to elucidate the nature of the interactions that control the binding process.

2 Computational details

2.1 Initial structures

A truncated pore model of the $Na_v1.4$ channel was constructed in VMD[28] based on the cryo-electron microscopic structure file of the channel in complex with its β1 subunit (PDB ID: 6AGF).[26] The α subunit of this channel is made from one long protein domain containing four homologous domains labelled DI to DIV. Each of these contains 6 transmembrane helices S1–S6 with S1–S4 forming independent voltage sensing domains and the S5–S6 of all four domains forming a single central pore. The simulation system comprised segments S5 and S6 of all four domains DI–DIV (residue index ranges: I: 234–286; 336–451, II: 683–805, III: 1143–1298, IV: 1464–1601) of the α subunit.

The protein was aligned along the *z*-axis using the Orientations of Proteins in Membranes (OPM) database and the Positioning of Proteins in Membrane (PPM) web server.[29] After amidating and acetylating N- and C-end groups, the structure was placed inside a 1-palmitoyl-2-oleoyl-*sn*-glycero-3-phosphocholine (POPC) lipid bilayer (*xy* length: 100 × 100 lipid components), as schematically representd in Fig. 1a, and solvated in a rectangular box with aqueous solvent and NaCl at a concentration of 0.15 mol L^{-1} (box dimensions: *x*: 95.5 Å, *y*: 95.5 Å, *z*: 117.2 Å). This was done using the CHARMM-GUI Bilayer Builder.[30–33] The potential parameters for the protein and lipids were taken from the CHARMM36m force field,[4] and the TIP3P model was employed for the water molecules.[34–36] Lennard-Jones parameters for ions were adopted from Joung and Cheatham.[37]

The ligands AZ and *p*-DAZ (see Fig. 1b) in the *trans* conformation were constructed using CHARMM-GUI Ligand Reader and Modeler.[38,39] The ligand force constants for the dihedral angles –C–N=N–C– and C–C–N=N– were taken from a previous work,[40] while the rest of the parameters were taken from CGenFF.[41] The geometry of the two photoswitches was optimized at MP2/6-31G* level of theory. This geometry was employed in the calculation of the restrained electrostatic potential (RESP) charges at the Hartree–Fock/6-31G* level of theory – to be consistent with the rest of the force field – and as initial geometry in the dynamic simulations described below.
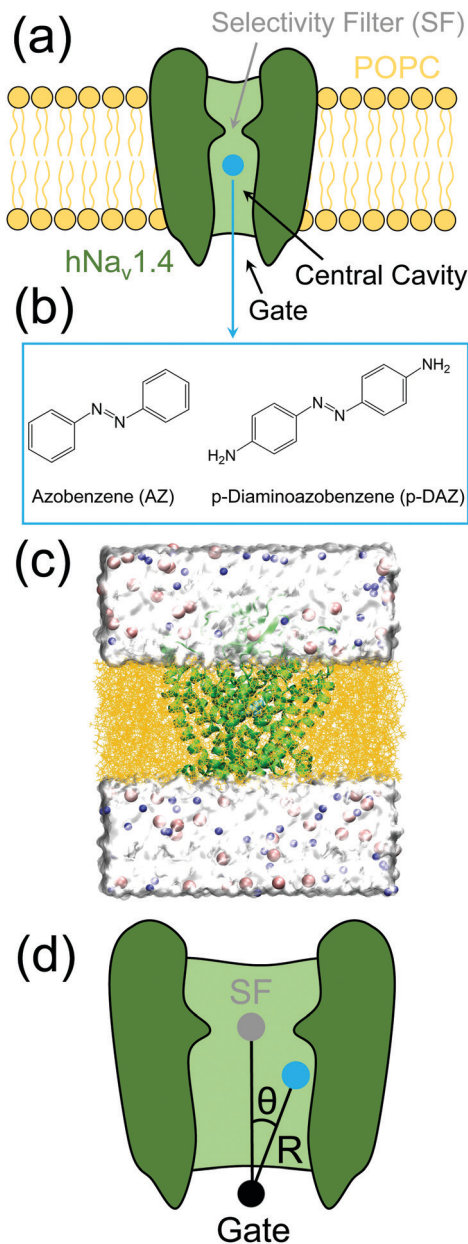
This journal is © the Owner Societies 2021

Phys. Chem. Chem. Phys., 2021, **23**, 3552–3564 | **3553**

Fig. 1 (a) Schematic representation of the human Na$_V$1.4 channel (green) integrated into a solvated POPC bilayer (yellow) with a photoswitch (cyan circle) interacting with the protein inside its central cavity. (b) Chemical formula of the two photoswitches investigated, namely, azobenzene (AZ) and p-diamino-azobenzene (p-DAZ). (c) VMD representation of the initial snapshot for the AZ simulation. AZ is displayed as cyan van der Waals spheres, the channel as a green cartoon, the lipid membrane as yellow lines, the water as a white surface, and the sodium and chloride ions as blue and pink spheres, respectively. (d) Reaction coordinates employed to represent the free-energy surface: Distance R between the centers of mass of the photoswitches (cyan circle) and of the gate (black circle), and angle θ formed by the centers of mass of the photoswitch, of the gate and of the selectivity filter (grey circle). The center of mass of the gate is defined as the center of mass of the α carbons of residues Val446, Leu800, Val1293, and Ile1596 located at the gate. The center of mass of the selectivity filer is defined as the center of mass of the α carbons of the residues that compose the so-called DEKA filter, namely, Asp406, Glu761, Lys1244, and Ala1536.

The quantum mechanical calculations were conducted with the Gaussian16 package.[42] Both ligands were inserted at the

center of mass of the channel, inside the central cavity (see Fig. 1a and c). Two systems composed of Na$_V$1.4 with AZ and p-DAZ were arranged inside a solvated and ionised POPC lipid bilayer using the CHARMM-GUI membrane builder as described above.

2.2 Conventional molecular dynamics simulations

Conventional molecular dynamics (cMD) simulations for the solvated membrane-protein system without the ligands were performed using NAMD.[43] Initially, the energy was minimized for 10 000 steps. Then, subsequent simulations were run in the isothermal–isobaric ensemble (*NPT*) at 303.15 K and 1.01 bar with a timestep of 2 fs. Hydrogen bond lengths were kept fixed using the SHAKE algorithm.[44] The van der Waals cutoff radius, switching distance and pairlist distance were set at 12.0 Å, 10 Å and 16.0 Å, respectively. Electrostatic interactions were calculated using the particle-mesh Ewald method with a grid spacing of 1.0 Å.[45] The system was equilibrated in six decreasingly restrained simulations of 2.5×10^6 timesteps (5 ns) each (see Table 1). Temperature and pressure were controlled with the Langevin thermostat (damping coefficient 1 ps^{-1}) and barostat (piston period 100 fs in run 1–2 and 50 fs in run 3–6, piston decay 50 fs in run 1–2 and 25 fs in run 3–6). Harmonic restraints were imposed on the protein backbone (scaling factor = 1) and on side chain carbon atoms (scaling factor = 0.5). Additional dihedral and improper restraints were placed on selected atoms inside the lipid atoms and lipid heads in the membrane were harmonically restrained to the *xy*-plane. Table 1 lists the values of the force constants of each run. Then, an unconstrained production run was performed for 150 ns.

After the cMD simulations for the membrane-protein system, the ligands were inserted in the model and additional cMD simulations were performed with the CUDA version[46] of the AMBER18 package.[47] First, an energy minimization was carried out with the steepest descendent method for 2500 steps followed by conjugate gradient method for 2500 steps. The van der Waals cutoff radius and switching distance were set to 12.0 Å and 10.0 Å, respectively. Positional restraints were applied for amino acid residues and for membrane lipids along the heating and equilibration. The restraint force constants used along the dynamics protocol are listed in Table 2. An *NVT* heating at 303.15 K over 125 ps was performed with the Langevin thermostat

Table 1 Force constants of restraints placed on lipid and protein atoms during equilibration runs

Run	Protein restraints	Lipid restraints	
		Dihedral and improper	Planar
1	10.0	500	5.0
2	5.0	200	5.0
3	5.0	100	2.0
4	2.0	100	1.0
5	0.5	50	0.2
6	0.1	0	0.1

Force constants (kcal mol^{-1} Å^{-2} or kcal mol^{-1} rad^2)

3554 | *Phys. Chem. Chem. Phys.*, 2021, **23**, 3552–3564

This journal is © the Owner Societies 2021

Table 2 Force constants of positional restraints placed on lipid and protein atoms during equilibration runs

Run	Force constants (kcal mol−1)	
	Protein restraints	Lipid restraints
1 (*NVT*)	10	2.5
2 (*NVT*)	5	2.5
3 (*NPT*)	2.5	1.0
4 (*NPT*)	1.0	0.5
5 (*NPT*)	0.5	0.1
6 (*NPT*)	0.1	0.0

Table 3 cMD and GaMD simulation stages

Stages of GaMD algorithm	Time (ns)	
	AZ	*p*-DAZ
cMD equilibration	2	2
cMD parameters collection	8	8
GaMD equilibration	5	5
GaMD updated statistics	35	35
GaMD production	4×1000	4×1000

(friction coefficient 1.0 ps) in two steps with different constraints and with a 1.0 fs timestep. Then, the desired density was achieved by running an equilibration in the *NPT* ensemble with a Monte Carlo barostat and a semiisotropic pressure scaling, once for 125 ps with a 1 fs timestep and three times for 500 ps with a 2 fs timestep. Electrostatic interactions were calculated by means of the particle-mesh Ewald method with a grid spacing of 1.0 Å, and hydrogen bond lengths were kept fixed using the SHAKE algorithm. Finally, an unconstrained production run was carried out at 303.15 K and 1.01 bar for 200 ns.

2.3 Gaussian accelerated molecular dynamics simulations

The binding of photoswitches to ion channels and the transition between different binding sites – likely separated by relatively high-energy barriers – are slow events. The simulation of such events requires the use of enhanced-sampling techniques that accelerate the dynamics. Many enhanced-sampling methods that apply a bias potential along one or more reaction coordinates have been developed.[48] However, their use is not always possible because it requires a deep knowledge of the process under investigation to properly define the reaction coordinates. In the situations where such a knowledge is not available, as it is the case here, it is necessary to employ other approaches that do not need the predefinition of reaction coordinates, such as GaMD.[27] GaMD simulations, where a harmonic boost potential is applied to smooth the potential-energy surface and reduce system barriers, were performed using the CUDA version of the AMBER18 package.[46,47] The initial position of the ligands was taken from the last snapshot of the previous 200 ns cMD equilibration, in which the ligands were initially placed at the center of mass of the channel. The initial position of the photoswitches could also be guessed from docking simulations. However, since GaMD is able to efficiently explore the configurational space, previous docking simulations are not needed. In the following we use the notation employed by the authors who implemented the GaMD algorithm.[49]

The different steps of the GaMD simulations are summarized in Table 3. The GaMD starts with 2 ns of cMD equilibration. The system threshold energy is set as $E = V_{\max}$ and the values of the minimum ($V_{\min}$), maximum ($V_{\max}$), average (V_{av}) and standard deviation (σ_{V}) of the potential energy are then collected over 8 ns of cMD. Those statistics are required to calculate GaMD boost parameters. A dual boost on both dihedral and total potential

energy is applied and the GaMD protocol proceeds with a 5 ns equilibration stage, where the system potential statistics are updated to recalculate the GaMD acceleration parameters on the fly, and a 35 ns simulation to reach a maximum value for the effective harmonic force constants, k_{0D} and k_{0P}, of the dihedral and total potential-energy boost and, thus, enable the highest acceleration. For both AZ and *p*-DAZ systems, four replicate production GaMD simulations of 1000 ns each were performed. Two reaction coordinates were defined for the reweighting of the GaMD free energy surfaces, as shown in Fig. 1d. First, the center of mass of the ligand, the center of mass of the α carbons of the protein DEKA filter (Asp406, Glu761, Lys1244, Ala1536), and the center of mass of the α carbons of the protein intracellular gate (Val446, Leu800, Val1293, Ile1596) were obtained, and the vector distances between these three points were calculated using the *cpptraj* tool.[50] The first reaction coordinate was set as the distance from the gate to the ligand, while the second reaction coordinate was set as the angle between the vectors from the gate to the ligand and from the gate to the DEKA filter. Reweighting of the GaMD free energy surfaces along the reaction coordinates were performed with the *PyReweighting* toolkit employing a 10th-order Maclaurin series.[27] The calculation of the free-energy surface and the visualization of the dynamics allowed the identification of different binding pockets for AZ and *p*-DAZ, as discussed below.

2.4 Free-energy surfaces and binding free energy

After identifying the binding pockets, the binding free energies of AZ/Na$_{\mathrm{V}}$1.4 and *p*-DAZ/Na$_{\mathrm{V}}$1.4 for each of the pockets were calculated with the one-average molecular-mechanics generalized Born surface-area (1A-MM-GBSA) approach.[51,52] First, an additional 100 ns cMD for each of the pockets were run after the GaMD productions to confirm the stability of the ligand binding inside the potential pockets and estimate the total binding free energy. For the binding pockets for which the complex does not dissociate MM-GBSA calculations were carried out using the MMPBSA.py tool.[53] As discussed later, the convergence of the binding free energy was analyzed in terms of the computational time and number of frames to find a good balance between precision and computational effort. The analysis showed that the selection of 100 equidistant frames from each simulated trajectory of 100 ns is sufficient to obtain converged energies. The MM-GBSA method uses the generalized Born (GB) approach for the calculation of the polar solvation energy, which represents the electrostatic interaction between the ligand/protein complex and the continuum

This journal is © the Owner Societies 2021

Phys. Chem. Chem. Phys., 2021, **23**, 3552–3564 | **3555**

solvent, with a NaCl concentration of 0.15 M. The nonpolar solvation energy, which includes the cavitation energy and the dispersion and repulsion interactions between the ligand/ protein complex and solvent, was calculated using the solvent accessible surface area (SASA) approach.[51,52] In addition, a pairwise residue free-energy decomposition analysis was performed to obtain the contribution of each residue to the total binding free energy.[53] This decomposition was performed for the aminoacids which are located within a sphere of 5.0 Å radius from the photoswitch for at least 2% of the simulation. Then, the ten residues with the highest free-energy contribution are selected and discussed.

3 Results

3.1 Characterization of binding pockets

As explained above, the first step of the simulation protocol was to run a 150 ns cMD trajectory with the $Na_V1.4$ channel integrated into a solvated POPC bilayer (in the absence of the photoswitches) to equilibrate the structure of the channel. Then, the photoswitches were placed at the centre of mass of the channel, which is located inside the central cavity, and one additional equilibration simulation was evolved for each ligand/channel system for 200 ns. The root mean-square displacement of the non hydrogen atoms of the protein along the cMD simulations in absence and in the presence of the photoswitches are represented in Fig. 2a. As can be seen, for the initial 150 ns simulation, the internal motion of the protein is relatively stabilized after 60 ns, although a slightly steady increment of the RMSD is still observed until the end of the simulation. This indicates that a full conformational equilibration has not been achieved yet. However, such a full equilibration is obtained along the subsequent 200 ns cMD simulations, where the two photoswitches are integrated inside the cavity of channel. As can be seen, the RMSD reaches a plateau after the first 100 ns for both simulations. The 200 ns equilibration is also important to find stable orientations of the ligands inside the cavity of the channel. As shown in Fig. 2b, after strong RMSD oscillations along the first 20 ns, the ligands reached energetically favourable orientations inside the channel. Specifically, the RMSD of AZ presents three stable regions around values of 17, 14 and 9 Å, while p-DAZ shows a clear stable position with RMSD of 10 Å with respect to the first snapshot. These orientations are good initial guesses for the subsequent GaMD simulations. The coordinates from the last snapshot of the cMD simulations were chosen as initial coordinates for four independent GaMD simulations for each of the ligands, where the initial velocities are freshly taken from a Boltzmann distribution at 303.15 K. Each of the GaMD simulations was evolved for 1 μs, i.e., the binding pockets for each of the ligands were searched for 4 μs. The free-energy surfaces obtained for AZ and p-DAZ interacting with the channel from the GaMD trajectories are plotted in Fig. 2c and d. As can be seen, the free-energy surfaces are similar for both ligands. However, it is important to note that this does not
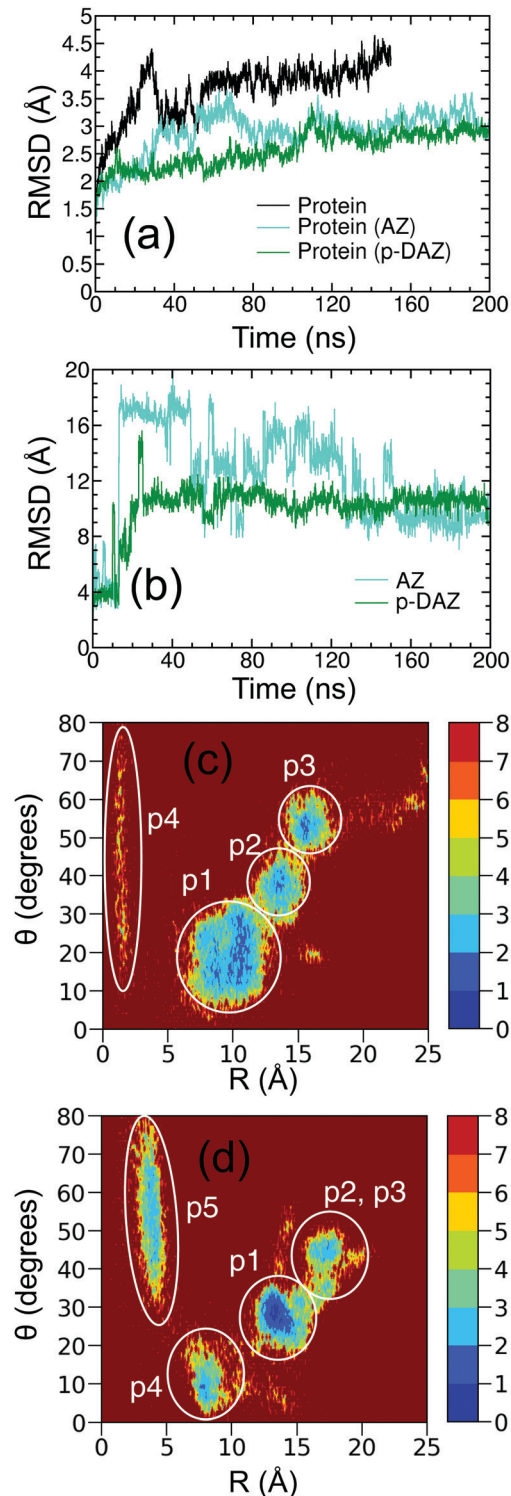

Fig. 2 (a) Root mean squared displacement (RMSD) of the non hydrogen atoms of the the human $Na_V1.4$ channel for the 150 ns equilibration cMD simulation in the absence of photoswitch (black) and for the 200 ns equilibration cMD simulations where the channel interacts with AZ (light blue) and p-DAZ (green). (b) RMSD of AZ (light blue) and p-DAZ (green) for the 200 ns equilibration cMD simulations. Binding pockets for (c) AZ and (d) p-DAZ on the free-energy surfaces computed from the GaMD simulations.

mean that both ligands visit the same regions of the central cavity of $Na_V1.4$. The contour plots shown in Fig. 2c and d are

3556 | Phys. Chem. Chem. Phys., 2021, 23, 3552–3564

This journal is © the Owner Societies 2021

only 2-dimensional cuts of the multidimensional free-energy surfaces, and although the two arbitrarily selected reaction coordinates present similar values for both ligands, many other coordinates may present very different values. Therefore, the characterization of the binding pockets should be carried out not only by exploring the cuts of the free-energy surfaces but also by visualization of the trajectories.

Fig. 2c reveals that four protein binding pockets were found for AZ in the GaMD simulations (p1, p2, p3 and p4). In the pockets p1 and p2 the photoswitch AZ is located between the domains DII and DIII of Na$_V$1.4, as displayed in Fig. 3a–c, where one representative snapshot for each binding pocket is shown. The main difference between these two pockets is that AZ is found closer to DIII in the pocket p1, while it is closer to DII in the pocket p2. The photoswitch is also interacting with DII and DIII in the pocket 3, but in this case AZ is inside a fenestration, *i.e.*, a lateral cavity of the channel relatively close to the nonpolar lipid bilayer. Pocket 4 is located at the gate of the channel as indicated by the small values of the reaction coordinate R on the free-energy contour plot (Fig. 2c). In this region, the ligand is interacting with residues of the protein domains DII, DIII and DIV. However, this minimum of the free-energy surface is not deep and, therefore, it is less populated by the ligand than the other 3 binding pockets. In fact, the complex formed by AZ and the residues of the gate is not stable as will be discussed later.

In the case of the photoswitch *p*-DAZ, five different pockets (p1 to p5) have been identified on the free-energy surface, shown in Fig. 2d. Representative snapshots for each of the pockets are displayed in Fig. 3d–f. In the pocket p1 the ligand is oriented in three different poses between the protein domains DIII and DIV. However, the three poses present similar features and, therefore, only one of them will be discussed and analyzed in detail below. In the pockets p2 and p3, *p*-DAZ is located inside a fenestration. However, the cavity is different for each pocket: it is found between the domains DII and DIII for the pocket p2 and between DI and DII for the pocket p3. There are two binding pockets close to the intracellular gate, namely p4 and p5. In the former the photoswitch interacts with the domains DI, DII and DIII, while in the latter the photoswitch
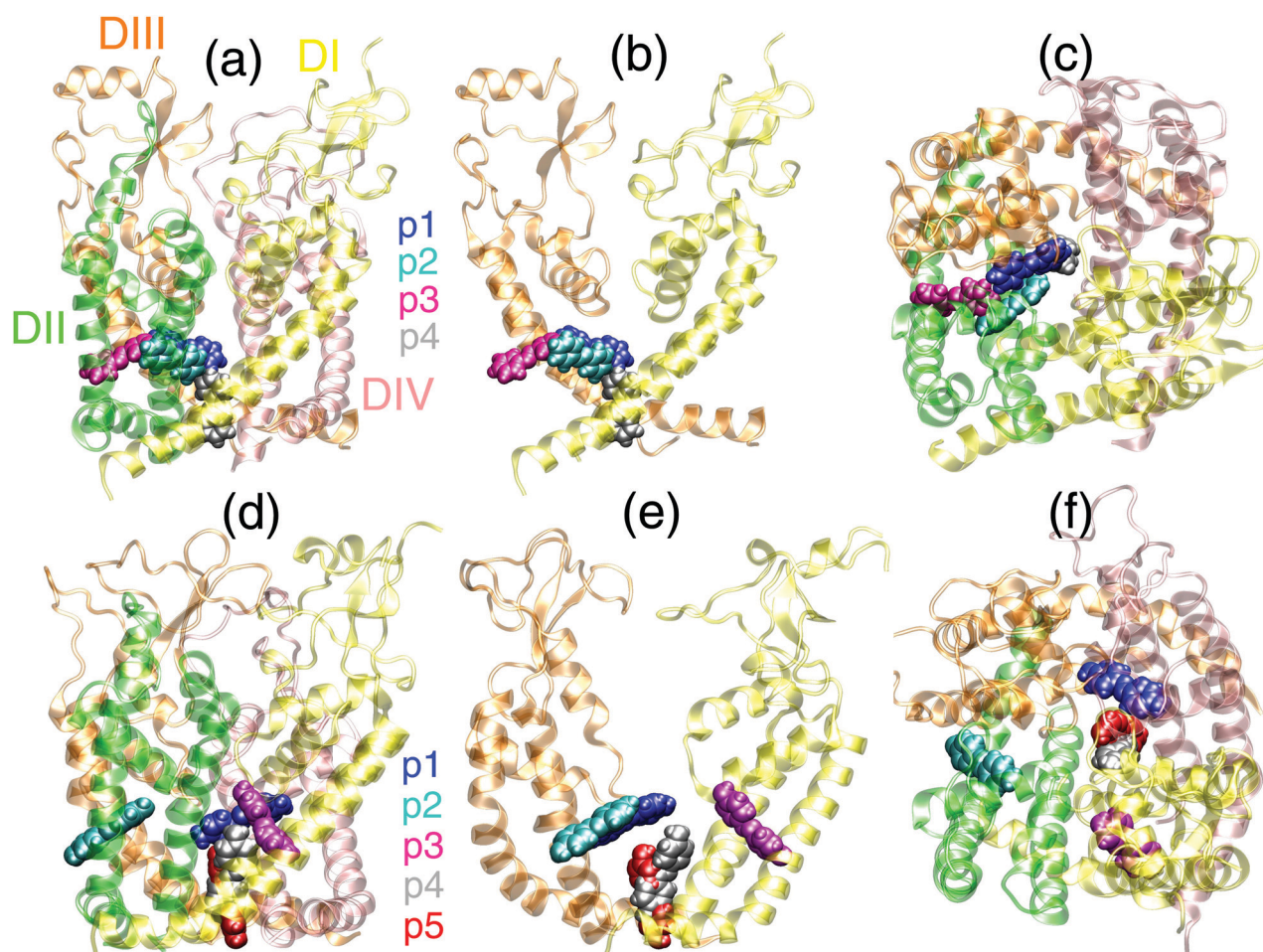

Fig. 3 One representative snapshot for each of the binding pockets of (a–c) AZ and (d–f) *p*-DAZ on the human Na$_V$1.4 channel from different perspectives. The panels (a) and (d) are side views from the plane of the lipid membrane where the the four protein domains are shown, while the panels (b) and (e) display a similar side view but from a different orientation and only the DII and DIV domains are shown. The panels (c) and (f) show a top down view. The photoswitches located in the binding pockets p1, p2, p3, p4 and p5 are shown in blue, cyan, magenta, grey and red, respectively.

This journal is © the Owner Societies 2021

Phys. Chem. Chem. Phys., 2021, **23**, 3552–3564 | **3557**

is more symmetrically centered with respect to the protein pore and is able to interact with residues from the four domains. The comparison of the two sets of pockets obtained from the GaMD simulations for both ligands states that the pockets p2 and p5 for *p*-DAZ are equivalent to the pockets p3 and p4 for AZ, respectively. The examination of Fig. 2c and d enables to draw some clear differences in the binding behaviour of both photoswitches. The free-energy surface for AZ is relatively flat throughout the minima associated to the pockets p1, p2 and p3 and, thus, these three pockets are evenly populated by the ligand. Moreover, the relevance of pocket p4 is only marginal. Contrary, the p5 pocket for *p*-DAZ is much more populated than the analogous p4 pocket for AZ. In addition, the free-energy surface is rougher and presents a clear favoured binding site at the pocket p1. These conclusions will be corroborated in the next section by the estimation of the binding free energy for each of the pockets. The differences found in the binding patterns of AZ and *p*-DAZ suggest that both ligands likely have a different mode of action when interacting with the channel. In fact, as discussed later, it is found that the *p*-DAZ ligand behaves as a classical local anaesthetic drug, while this is not the case for AZ.

The different pockets discussed above can also be identified by analyzing the motion of the ligands inside the internal cavity of the ion channel. Fig. 4 displays the RMSD of the photoswitches along the four GaMD trajectories evolved for each of the ligands. In the case of AZ (see Fig. 4a–d), pockets 1 and 2 are

populated in four and three trajectories, respectively, for long simulation times. Pocket p3 is present in two trajectories for shorter time. It is also interesting to notice that in the replica R3 the photoswitch leaves the channel from the pocket 3 through a lateral fenestration, reaching the lipid membrane. This indicates that ligands of similar size as AZ do not need to travel through the gate to enter the channel since they are able to diffuse through lateral fenestrations accessible from the membrane. However, additional simulations and analyses would be necessary to corroborate this. Pocket p4 is only populated in the trajectory R1 for around 100 ns. The most important binding site for *p*-DAZ (see Fig. 4e–h) is the pocket p1, which is populated by the ligand in three trajectories for long periods of time, especially in the replica 4 where the binding mode is preserved along the entire simulation. The other binding modes are present only in one of the trajectories. However, the interaction between *p*-DAZ and the protein is likely strong for the pocket p5 since this binding mode lasts for more than 600 ns. Although different binding sites than those found here could exist, the population of the same pockets several times across the trajectories and/or the population of the pockets for very long times suggest that the GaMD simulations have found the most relevant binding sites for the two ligands: pockets p1 and p2 for AZ and pockets p1 and p5 for *p*-DAZ. This will be confirmed in the next section by the estimation of the binding free energies by means of the MM-GBSA approach.

3.2 Binding Free Energy and Pairwise Residue Decomposition

Once the different pockets for AZ and *p*-DAZ are identified, the ligand/protein binding free energy for each of them is computed by the 1A-MM-GBSA approach to assess which of the pockets is the preferred binding site from a thermodynamic point of view. The use of this class of continuum approaches has been widely employed to investigate ligand/biomolecule recognition.[54,55] To this aim, unbiased cMD simulations, for which one snapshot from each of the pockets is taken as initial conditions, were run for 100 ns. Among the four pockets where AZ binds to the channel, the complex AZ/Na$_V$1.4 was stable for three of them, namely p1, p2 and p3, while it dissociates for p4. In the case of *p*-DAZ, the complex was stable for the pockets p1, p3 and p5, and it dissociates during the cMD simulations for p2 and p4. Therefore, the binding free energy and its pairwise decomposition was performed for a total of six binding pockets. In order to evaluate the amount of simulation time and the number of snapshots that must be considered in the free-energy computation to obtain converged results, a convergence analysis was performed for the binding pocket p5 of the ligand *p*-DAZ, see Fig. 5. First, the binding free energy was computed by considering a different number of equidistant frames across the 100 ns cMD simulation. As can be observed, the free energy is converged when 100 snapshots are taken into account in the calculation. From 100 to 1000 frames the oscillation in the free energy is only around 0.2 kcal mol^{-1}. Then, in order to analyze the convergence with respect to the simulation time, 100 equidistant frames were selected from different time ranges

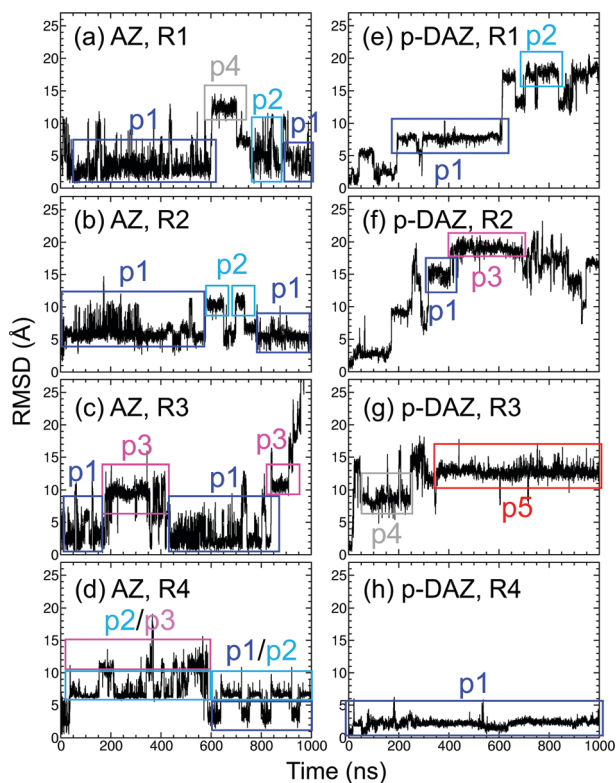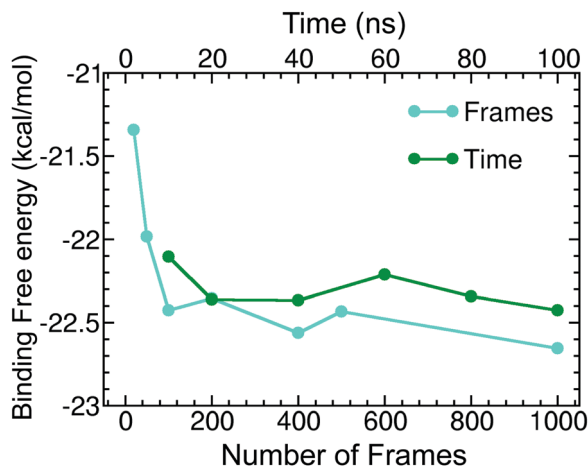**Fig. 4** RMSD of (a–d) AZ and (e–h) *p*-DAZ along the four GaMD replicas *R1–R4*.

Fig. 5 Variation of the binding free energy of *p*-DAZ inside the binding pocket 5 of the Na$_V$1.4 channel with time and number of snapshots.

along the simulation, namely, 10, 20, 40, 60, 80 and 100 ns. Fig. 5 shows that the variation of the free energy with respect to the simulation time is not important and, therefore, the simulations do not need to be extended for a longer time. Thus, in the following, the binding free energies for both ligands inside the different protein pockets were computed by selecting 100 equidistant frames across the 100 ns cMD simulations.

Table 4 lists the binding energies (ΔG_{total}) for the different pockets and their decomposition into four different components: van der Waals (ΔG_{vdw}) and electrostatic (ΔG_{el}) interactions between the ligand and the protein, polar solvation energy (ΔG_{pol}) and nonpolar solvation energy (ΔG_{np}). The polar solvation energy accounts for the difference between the ligand–protein–complex/solvent electrostatic interactions and the ligand/solvent and protein/solvent electrostatic interactions when the complex is dissociated. The nonpolar solvation energy considers the cavitation energy and the difference between the ligand–protein–complex/solvent respulsion and dispersion interactions and the ligand/solvent and protein/solvent respulsion and dispersion interactions when the complex is dissociated.[56] As can be seen, the binding of AZ into the pocket p2 of the channel, where the ligand interact with the DII and DIII domains of the protein, presents the most favorable binding energy (-19.4 kcal mol^{-1}). In the case of *p*-DAZ the most favorable

binding pocket is p1 ($-25,8$ kcal mol^{-1}), where the photoswitch is located between the DIII and DIV protein domains. The preferred pockets for both ligands are located close to the selectivity filter of the channel, in agreement with previous docking simulations and X-ray structural data for quaternary ammonium ligands interacting with the central cavity of K$^+$ channels.[23–25] The binding of drugs with protonated amino groups at the bottom of the selectivity filter was also found for the bacterial Na$_v$Ms and eukaryotic Na$_v$PaS channels by means of dynamic simulations,[57] and for the human Na$_v$1.5 channel by means of cryoelectron microscopy.[58] This type of binding close to the selectivity filter likely leads to the direct inhibition of the channel by blocking the pore. However, the favorable binding energies of the other binding sites predicted by our simulations, for example, inside fenestrations located between different protein domains, indicate that the two photoswitches investigated here could also participate in other class of inhibition mechanisms. For example, the binding of the ligands can stabilize the inactive state of the channel and prevent recovery to the closed state or opening of the gate as previously reported for different blockers.[59] Thus, different ion-blocking mechanisms can simultaneously operate. In addition, it is important to note that the binding process has been simulated for the ion channel in the inactivated state. However, a different activation state of the protein could result in different binding modes. The binding of *p*-DAZ to the protein is stronger than the binding of AZ and not only because of the larger size of *p*-DAZ, with the consequent larger number of interatomic interactions, but also because these interactions are stronger. This can be corroborated by normalizing the binding energies with respect to the number of atoms. For example, the normalized binding energy per atom for AZ into p2 and *p*-DAZ into p1 are 0.81 kcal mol^{-1} and 0.92 kcal mol^{-1}, respectively. The estimated binding energies qualitatively agree with the free-energy surfaces obtained from the GaMD simulations shown in Fig. 2c and d. The binding free energy difference between the preferred pocket (p2 for AZ and p1 for *p*-DAZ) and the other two pockets is smaller for AZ than for *p*-DAZ in agreement with the flatter free-energy surface obtained for AZ.

Table 4 reveals that the most important contributions to the total binding energy are the favorable van der Waals interactions between the ligand and the protein and the unfavorable polar solvation energy. The fact that the polar solvation energy is positive means that the electrostatic interactions between the ligand/protein complex and the solvent are less attractive than the electrostatic interactions between the individual monomers and the solvent. In addition, the nonpolar solvation energy contributes in a favorable way to the binding process. In other words, the unfavorable cavitation energy and repulsive interactions between the complex and the solvent are surpassed by the attractive dispersion interactions between the complex and the solvent. Moreover, the electrostatic interactions between the ligand and the protein are more important for *p*-DAZ than for AZ. In fact, these interactions are responsible for the larger binding free energy found for *p*-DAZ than for AZ. This can be better understood by comparing, for example, the most favorable

Table 4 Binding free energy (ΔG_{total}) of AZ and *p*-DAZ to the Na$_v$1.4 channel for the different protein pockets and decomposition into ligand/channel van der Waals (ΔG_{vdw}) and electrostatic (ΔG_{el}) interactions, and complex/solvent nonpolar (ΔG_{np}) and polar (ΔG_{pol}) interactions in kcal mol^{-1}

	AZ			*p*-DAZ		
	p1	p2	p3	p1	p3	p5
ΔG_{vdw}	-24.6	-29.5	-31.2	-32.3	-32.1	-31.7
ΔG_{el}	0.2	-0.8	-2.3	-6.4	-8.7	-2.4
ΔG_{np}	-3.5	-4.1	-4.4	-4.1	-4.7	-4.3
ΔG_{pol}	10.6	15.0	22.3	17.0	26.8	16.0
ΔG_{total}	-17.3	-19.4	-15.6	-25.8	-18.7	-22.4

This journal is © the Owner Societies 2021

Phys. Chem. Chem. Phys., 2021, **23**, 3552–3564 | **3559**

pockets for AZ (p2) and *p*-DAZ (p1). When one goes from AZ/p2 to *p*-DAZ/p1 the ligand/protein van der Waals interactions increase (in absolute value) from −29.5 kcal mol⁻¹ to −32.3 kcal mol⁻¹, *i.e.*, there is an increase in the attractive interactions of 2.8 kcal mol⁻¹. This is compensated by an increase in the unfavorable polar solvation energy from 15.0 kcal mol⁻¹ for AZ/p2 to 17.0 kcal mol⁻¹ for p-AZ/p1. Since the nonpolar solvation energy does not change (−4.1 kcal mol⁻¹), the term which makes the binding of *p*-DAZ more favorable than the binding of AZ is the ligand/protein electrostatic interactions, which are more important for *p*-DAZ (−6.4 kcal mol⁻¹) than for AZ (−0.8 kc al mol⁻¹). As will be seen later, the importance of the ligand/protein electrostatic interactions for *p*-DAZ is a consequence of the presence of the amino groups on the *para* position of the benzene rings of the ligand (see Fig. 1b), which leads to interactions with polar residues of the channel – hydrogen bonding and long-range interactions – that are not present in the case of AZ.

To gain more insight into the nature of the ligand/protein interactions, the binding free energy for the three stable pockets of AZ and *p*-DAZ was decomposed into pairwise residue energies. The ten most important residue contributions are listed in Fig. 6.

In addition, the three residues that present the most important contribution to the binding energy for each of the pockets are represented in Fig. 7. In the following discussion we will use the same residue notation as that employed in ref. 26. The photo-switch AZ undergoes the strongest interactions with nonpolar residues of the ion channel, such as Phe(797, 1284, 1243, 1284), Leu1287, Val793 and Ile1280. In addition, the most important energy terms are the van der Waals interactions between AZ and the aminoacids and the nonpolar solvation energy. For example, for the most favorable binding pocket p2, the strongest contribution to the total binding energy comes from the Phe1243 residue of the protein domain D3, which interacts with AZ by means of stacking interactions, as can be seen in Fig. 7b. In the case of *p*-DAZ, the photoswitch/protein complex is also stabilized by interactions with nonpolar aminoacids, *e.g.*, Phe1586, Leu250, Ile1295 and Val1590, where the ligand/amino acid van der Waals and nonpolar solvation terms dominate the total free energy, as in the case of AZ. The importance of nonpolar protein residues has also been found for the tetrabutylammonium ligand bind to the KcsA potassium channel,[24] for which the binding of the ligand was stabilized by interactions with the side chains of Phe
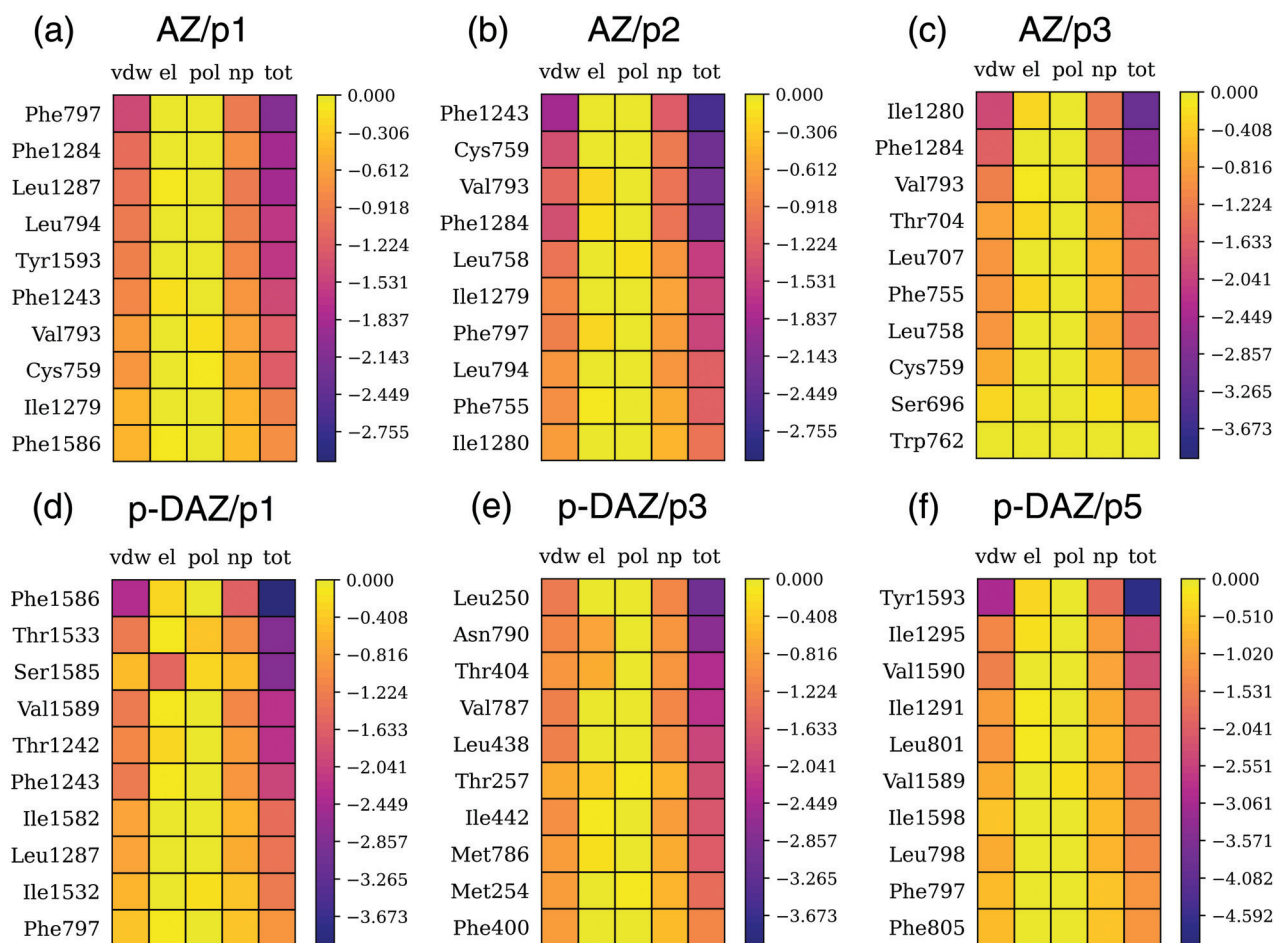

Fig. 6 Pairwise residue decomposition of the binding free energy for the pockets (a) p1, (b) p2 and (c) p3 of AZ and (d) p1, (e) p3 and (f) p5 of *p*-DAZ. Each residue contribution is in turn decomposed into ligand/protein van der Waals (vdW) and electrostatic (el) contributions and polar (pol) and nonpolar (np) solvation contributions to the total residue binding energy (tot).
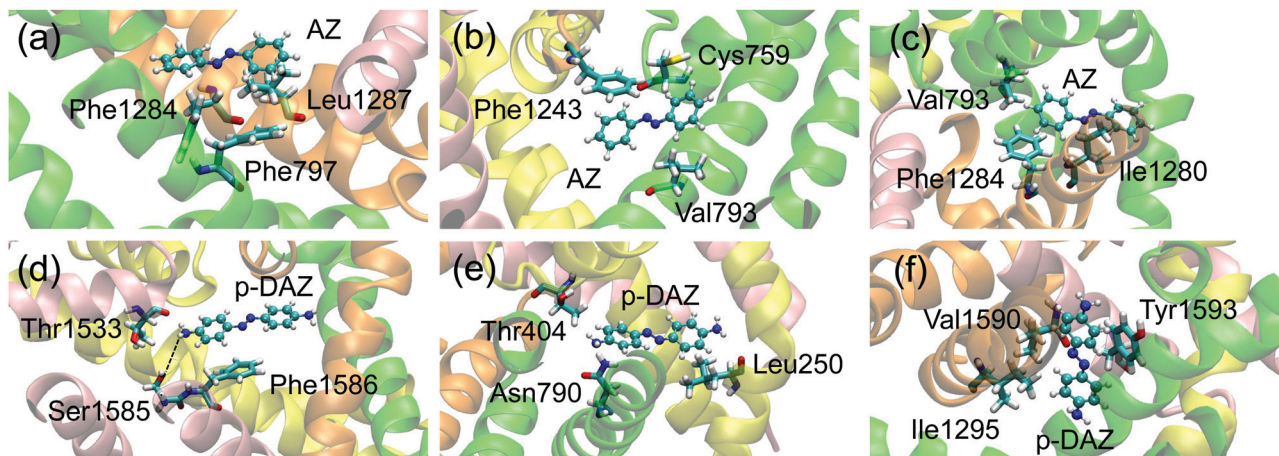
Fig. 7 Representation of the three aminoacids that present the most important contribution to the binding free energy for the pockets (a) p1, (b) p2, and (c) p3 of AZ and the pockets (d) p1, (e) p3, and (f) p5 of *p*-DAZ. The aminoacids and the ligands are shown in licorice and CPK (balls and sticks) representations, respectively. Color code for atoms: cyan for C, red for O, blue for N, yellow for S, and white for H.

and Ile residues. However, despite the importance of hydrophobic interactions, the photoswitch *p*-DAZ also undergoes intermolecular interactions with polar residues of the channel, such as Ser1585, Asn790, Thr(1533, 404) and Tyr1593, where the electrostatic interactions are significant. For example, as seen in Fig. 6d, the strongest contributions to the total binding energy for the pocket p1 of *p*-DAZ comes from the nonpolar residues Phe1586, but also from the polar residues Thr1533 and Ser1585. The electrostatic contribution from the last one is relatively high. The visualization of the dynamics for this pocket reveals that part of this electrostatic energy is caused by hydrogen bonding, where one of the amino groups of *p*-DAZ acts as hydrogen donor and the OH group of the side chain of Ser1585 acts as hydrogen acceptor, as can be seen in Fig. 7d. For the pocket p3, the electrostatic term is important for the polar aminoacids Asn790 and Thr404, (Fig. 6e). For the pocket p5, Tyr1593 also presents an important electrostatic component (Fig. 6f), although less pronounced than that of the polar residues from the other two pockets. The residues that contribute most to the binding free energy of the two most favorable pockets p1 and p5 for *p*-DAZ are Phe1586 and Tyr1593, respectively, located in the D4 domain. These two aminoacids – especially Phe1586 – have been previously identified as key residues for the binding of local anaesthetic drugs to the human Na$_v$1.4 channel[60,61] and other voltage-gated Na$^+$ channels.[62] Thus, the photoswitch *p*-DAZ behaves, at least partially, as a classical local anaesthetic drug.

A quantitative hydrogen bond analysis for the polar residues involved in the interactions with *p*-DAZ was performed: Thr1533, Ser1585 and Thr1242 in pocket p1; Asn790, Thr404 and Thr257 in pocket p3; and Tyr1593 in pocket p5. It was assumed that a hydrogen bond is formed when the distance between the hydrogen donor and the hydrogen acceptor atoms is shorter than 3.0 Å, and the angle formed by the hydrogen donor, hydrogen, and hydrogen acceptor atoms is larger than 135°, which are arbitrary structural criteria commonly used in the literature.[63,64] The hydrogen bond between *p*-DAZ and Ser1585 described above for the pocket p1 (see Fig. 7d) is

present along 42% of the simulation time. However, the photoswitch only interacts sporadically (less than 5% of the simulations time) by hydrogen bonding with the polar aminoacids within the pockets p3 and p5. This means that the strong electrostatic interactions present in the pocket p3 and, in less extent, in the pocket p5 are of long-range character.

4 Conclusions

Molecular photoswitches have been developed over the last decades in the field of photopharmacology to enhance the selectivity of medical treatments with the help of the high spatiotemporal resolution that can be achieved by the use of light. Specifically, it has been shown that ion conduction through voltage-gated ion channels can be modulated by the binding of AZ derivatives to the internal cavity of the channel and subsequent irradiation with light. The characterization of the protein binding pockets involved in this process is crucial to unveil the nature of the interactions that leads to an efficient blockage of the activity of the channel, and to investigate the effect of the protein environment on the photophysics of the photoswitches.

In this work, the binding of AZ and *p*-DAZ to the human Na$_v$1.4 channel was modelled by means of GaMD simulations and the binding free-energy was computed by the 1A-MM-GBSA approach. We have identified three binding pockets for AZ, which are located between the domains DII and DIII. The two most stable pockets are inside the internal cavity of the protein relatively close to the selectivity filter, while the third one is inside a lateral fenestration close to the lipid membrane. The binding of AZ is largely controlled by hydrophobic interactions with nonpolar residues of the channel, especially with Phe, Leu, Val and Ile aminoacids. These attractive interactions are partially counteracted by the unfavorable polar solvation energy. Three stable binding pockets were also identified for *p*-DAZ. The most thermodynamically favorable pocket was found

between the protein domains DIII and DIV inside the central cavity of the channel and close to the selectivity filter. The second most stable pocket is located on the intracellular gate of the channel, and the third pocket is inside a lateral cavity close to the bilayer between the domains DI and DII. As for AZ, the binding of *p*-DAZ to the protein is largely controlled by van der Waals interactions with nonpolar aminoacids and by the polar solvation energy. However, the complex is also stabilized by electrostatic interactions with polar residues. In the case of the most stable pocket, a large fraction of this electrostatic energy is caused by a hydrogen bond formed between the ligand and the Ser1585 residue, where one of the amino groups of *p*-DAZ plays the role of hydrogen donor. For the other two less favorable pockets, the electrostatic interactions are of long-range character since long-lasting hydrogen bonds are not formed along the simulation. The ligand *p*-DAZ behaves as a classical local anaesthetic when it interacts with the channel in the two most stable pockets p1 and p5. Overall, the photoswitch *p*-DAZ is able to bind to the channel in a stronger way than AZ. Moreover, although a preferred pocket for each of the ligands have been identified, it is very likely that both photoswitches are able to bind to more than one binding site.

The presence of different binding pockets inside the central cavity of the Na$_V$1.4 channel does not directly imply that the ligand binding will block the transport of ions through the protein. Although the fact that the preferred binding pockets occur close to the selectivity filter suggests that the behaviour of the channels will be altered by a direct blocking of the pore, future research needs to be performed to elucidate it. In addition, the binding to sites located between protein domains indicate that the inhibition of the channel by stabilization of the inactive state could also be operative. It is also necessary to investigate the effect of the protein environment on the electronic structure and photophysics of the photoswitches. It is reasonable to state that the photoinduced isomerization mechanism and quantum yield are not the same in all the binding pockets because the protein environment that interacts with the photoswitches is different in each pocket. Works in these directions are currently in progress in our groups. The elucidation of the different factors involved in the photoisomerization and ion conduction processes will allow the design of efficient photoswitches aimed to modulate the activity of voltage-gated ion channels.

Conflicts of interest

There are no conflicts to declare.

Acknowledgements

Notes and references

1   M. A. Chisholm-Burns, *Pharmacotherapy principles & practice*, McGraw-Hill Medical, New York, 2008.
2   M. Lerch, M. Hansen, G. van Dam, W. Szymanski and B. Feringa, *Angew. Chem., Int. Ed.*, 2016, **55**, 10978–10999.
3   D. Huggins, W. Sherman and B. Tidor, *J. Med. Chem.*, 2012, **55**, 1424–1444.
4   W. Velema, W. Szymanski and B. Feringa, *J. Am. Chem. Soc.*, 2014, **136**, 2178–2191.
5   W. Szymański, J. Beierle, H. Kistemaker, W. Velema and B. Feringa, *Chem. Rev.*, 2013, **113**, 6114–6178.
6   A. Beharry and G. Woolley, *Chem. Soc. Rev.*, 2011, **40**, 4422–4437.
7   K. Hüll, J. Morstein and D. Trauner, *Chem. Rev.*, 2018, **118**, 10710–10747.
8   M. Fuchter, *J. Med. Chem.*, 2020, **63**, 11436–11447.
9   N. Ankenbruck, T. Courtney, Y. Naro and A. Deiters, *Angew. Chem., Int. Ed.*, 2018, **57**, 2768–2798.
10 J. Broichhagen, J. Frank and D. Trauner, *Acc. Chem. Res.*, 2015, **48**, 1947–1960.
11 H. Bandara and S. Burdette, *Chem. Soc. Rev.*, 2012, **41**, 1809–1825.
12 A. Blevins and G. Blanchard, *J. Phys. Chem. B*, 2004, **108**, 4962–4968.
13 C. Crecca and A. Roitberg, *J. Phys. Chem. A*, 2006, **110**, 8188–8203.
14 P. Bregestovski and G. Maleeva, *Neurosci. Behav. Physiol.*, 2019, **49**, 184–191.
15 P. Paoletti, G. Ellis-Davies and A. Mourot, *Nat. Rev. Neurosci.*, 2019, **20**, 514–532.
16 W. Catterall, *J. Physiol.*, 2012, **590**, 2577–2589.
17 S. Cannon, *Neurotherapeutics*, 2007, **4**, 174–183.
18 M. Zaydman, J. Silva and J. Cui, *Chem. Rev.*, 2012, **112**, 6319–6333.
19 J. J. Nogueira and B. Corry, *Ion Channel Permeation and Selectivity in The Oxford Handbook of Neuronal Ion Channels*, Oxford University Press, Oxford, 2018.
20 A. Mourot, T. Fehrentz, Y. Le Feuvre, C. Smith, C. Herold, D. Dalkara, F. Nagy, D. Trauner and R. Kramer, *Nat. Methods*, 2012, **9**, 396–402.
21 J. Trads, K. Hüll, B. Matsuura, L. Laprell, T. Fehrentz, N. Görldt, K. Kozek, C. Weaver, N. Klöcker, D. Barber and D. Trauner, *Angew. Chem., Int. Ed.*, 2019, **58**, 15421–15428.
22 M. Banghart, A. Mourot, D. Fortin, J. Yao, R. Kramer and D. Trauner, *Angew. Chem., Int. Ed.*, 2009, **48**, 9097–9101.
23 A. Mourot, C. Herold, M. Kienzler and R. Kramer, *Br. J. Pharmacol.*, 2018, **175**, 2296–2311.
24 M. Lenaeus, M. Vamvouka, P. Focia and A. Gross, *Nat. Struct. Mol. Biol.*, 2005, **12**, 454–459.

3562 | *Phys. Chem. Chem. Phys.*, 2021, **23**, 3552–3564

This journal is © the Owner Societies 2021

25 M. Zhou, J. Morais-Cabral, S. Mann and R. MacKinnon, *Nature*, 2001, **411**, 657–661.

26 X. Pan, Z. Li, Q. Zhou, H. Shen, K. Wu, X. Huang, J. Chen, J. Zhang, X. Zhu, J. Lei, W. Xiong, H. Gong, B. Xiao and N. Yan, *Science*, 2018, **362**, 6412.

27 Y. Miao, W. Sinko, L. Pierce, D. Bucher, R. C. Walker and J. A. McCammon, *J. Chem. Theory Comput.*, 2014, **10**, 2677–2689.

28 W. Humphrey, A. Dalke and K. Schulten, *J. Mol. Graphics*, 1996, **14**, 33–38.

29 M. A. Lomize, I. D. Pogozheva, H. Joo, H. I. Mosberg and A. L. Lomize, *Nucleic Acids Res.*, 2012, **40**, D370–D376.

30 S. Jo, T. Kim, V. G. Iyer and W. Im, *J. Comput. Chem.*, 2008, **29**, 1859–1865.

31 J. Lee, X. Cheng, J. M. Swails, M. S. Yeom, P. K. Eastman, J. A. Lemkul, S. Wei, J. Buckner, J. C. Jeong, Y. Qi, S. Jo, V. S. Pande, D. A. Case, C. L. Brooks, A. D. MacKerell, J. B. Klauda and W. Im, *J. Chem. Theory Comput.*, 2016, **12**, 405–413.

32 E. L. Wu, X. Cheng, S. Jo, H. Rui, K. C. Song, E. M. Dávila-Contreras, Y. Qi, J. Lee, V. Monje-Galvan, R. M. Venable, J. B. Klauda and W. Im, *J. Comput. Chem.*, 2014, **35**, 1997–2004.

33 S. Jo, T. Kim and W. Im, *PLoS One*, 2007, **2**, e880.

34 R. B. Best, X. Zhu, J. Shim, P. E. M. Lopes, J. Mittal, M. Feig and A. D. MacKerell, *J. Chem. Theory Comput.*, 2012, **8**, 3257–3273.

35 J. B. Klauda, R. M. Venable, J. A. Freites, J. W. O'Connor, D. J. Tobias, C. Mondragon-Ramirez, I. Vorobyov, A. D. MacKerell and R. W. Pastor, *J. Phys. Chem. B*, 2010, **114**, 7830–7843.

36 W. L. Jorgensen, J. Chandrasekhar, J. D. Madura, R. W. Impey and M. L. Klein, *J. Chem. Phys.*, 1983, **79**, 926–935.

37 I. S. Joung and T. E. Cheatham, *J. Phys. Chem. B*, 2008, **112**, 9020–9041.

38 S. Jo, T. Kim, V. G. Iyer and W. Im, *J. Comput. Chem.*, 2008, **29**, 1859–1865.

39 S. Kim, J. Lee, S. Jo, C. L. Brooks III, H. S. Lee and W. Im, *J. Comput. Chem.*, 2017, **38**, 1879–1886.

40 M. McCullagh, I. Franco, M. A. Ratner and G. C. Schatz, *J. Am. Chem. Soc.*, 2011, **133**, 3452–3459.

41 K. Vanommeslaeghe, E. Hatcher, C. Acharya, S. Kundu, S. Zhong, J. Shim, E. Darian, O. Guvench, P. Lopes, I. Vorobyov and A. D. Mackerell Jr, *J. Comput. Chem.*, 2010, **31**, 671–690.

42 M. J. Frisch, G. W. Trucks, H. B. Schlegel, G. E. Scuseria, M. A. Robb, J. R. Cheeseman, G. Scalmani, V. Barone, G. A. Petersson, H. Nakatsuji, X. Li, M. Caricato, A. V. Marenich, J. Bloino, B. G. Janesko, R. Gomperts, B. Mennucci, H. P. Hratchian, J. V. Ortiz, A. F. Izmaylov, J. L. Sonnenberg, D. Williams-Young, F. Ding, F. Lipparini, F. Egidi, J. Goings, B. Peng, A. Petrone, T. Henderson, D. Ranasinghe, V. G. Zakrzewski, J. Gao, N. Rega, G. Zheng, W. Liang, M. Hada, M. Ehara, K. Toyota, R. Fukuda, J. Hasegawa, M. Ishida, T. Nakajima, Y. Honda, O. Kitao, H. Nakai, T. Vreven, K. Throssell, J. A. Montgomery, Jr., J. E. Peralta, F. Ogliaro, M. J. Bearpark, J. J. Heyd, E. N. Brothers, K. N. Kudin, V. N. Staroverov, T. A. Keith, R. Kobayashi, J. Normand, K. Raghavachari, A. P. Rendell, J. C. Burant, S. S. Iyengar, J. Tomasi, M. Cossi, J. M. Millam, M. Klene, C. Adamo, R. Cammi, J. W. Ochterski, R. L. Martin, K. Morokuma, O. Farkas, J. B. Foresman and D. J. Fox, *Gaussian ∼ 16 Revision C.01*, 2016, Gaussian Inc., Wallingford CT.

43 J. C. Phillips, R. Braun, W. Wang, J. Gumbart, E. Tajkhorshid, E. Villa, C. Chipot, R. D. Skeel, L. Kalé and K. Schulten, *J. Comput. Chem.*, 2005, **26**, 1781–1802.

44 J.-P. Ryckaert, G. Ciccotti and H. J. Berendsen, *J. Comput. Phys.*, 1977, **23**, 327–341.

45 T. Darden, D. York and L. Pedersen, *J. Chem. Phys.*, 1993, **98**, 10089–10092.

46 R. Salomon-Ferrer, A. Götz, D. Poole, S. Le Grand and R. Walker, *J. Chem. Theory Comput.*, 2013, **9**, 3878–3888.

47 D. Case, I. Ben-Shalom, S. Brozell, D. Cerutti, T. V. Cruzeiro III, T. Darden, R. Duke, D. Ghoreishi, M. Gilson, H. Gohlke, A. Goetz, D. Greene, R. Harris, N. Homeyer, S. Izadi, A. Kovalenko, T. Kurtzman, T. Lee, S. LeGrand, P. Li, C. Lin, J. Liu, T. Luchko, R. Luo, D. Mermelstein, K. Merz, Y. Miao, G. Monard, C. Nguyen, H. Nguyen, I. Omelyan, A. O. Ev, F. Pan, R. Qi, D. Roe, A. Roitberg, C. Sagui, S. Schott-Verdugo, J. Shen, C. Simmerling, J. Smith, R. Salomon-Ferrer, J. S. Ails, R. Walker, J. Wang, H. Wei, R. Wolf, X. Wu, L. Xiao, D. York and P. Kollman, 2018, *AMBER 2018*, University of California, San Francisco.

48 C. Abrams and G. Bussi, *Entropy*, 2014, **16**, 163–199.

49 Y. Miao, V. A. Feher and J. A. McCammon, *J. Chem. Theory Comput.*, 2015, **11**, 3584–3595.

50 D. Roe and T. Cheatham, *J. Chem. Theory Comput.*, 2013, **9**, 3084–3095.

51 J. Srinivasan, J. Miller, P. A. Kollman and D. A. Case, *J. Biomol. Struct. Dyn.*, 1998, **16**, 671–682.

52 P. A. Kollman, I. Massova, C. Reyes, B. Kuhn, S. Huo, L. Chong, M. Lee, T. Lee, Y. Duan, W. Wang, O. Donini, P. Cieplak, J. Srinivasan, D. A. Case and T. E. Cheatham, *Acc. Chem. Res.*, 2000, **33**, 889–897.

53 B. R. Miller, T. D. McGee, J. M. Swails, N. Homeyer, H. Gohlke and A. E. Roitberg, *J. Chem. Theory Comput.*, 2012, **8**, 3314–3321.

54 J. Nogueira and L. González, *Biochemistry*, 2014, **53**, 2391–2412.

55 C. Wang, D. Greene, L. Xiao, R. Qi and R. Luo, *Front. Mol. Biosci.*, 2018, **4**, 87.

56 S. Genheden and U. Ryde, *Expert Opin. Drug Discovery*, 2015, **10**, 449–461.

57 A. Buyan, D. Sun and B. Corry, *Proc. Natl. Acad. Sci. U. S. A.*, 2018, **115**, E3135–E3144.

58 D. Jiang, H. Shi, L. Tonggu, T. Gamal El-Din, M. Lenaeus, Y. Zhao, C. Yoshioka, N. Zheng and W. A. Catterall, *Cell*, 2020, **180**, 122–134.

59 W. A. Catterall and T. M. Swanson, *Mol. Pharmacol.*, 2015, **88**, 141–150.

This journal is © the Owner Societies 2021

Phys. Chem. Chem. Phys., 2021, **23**, 3552–3564 | 3563

60 J.-F. Desaphy, A. Dipalma, T. Costanza, R. Carbonara, M. Dinardo, A. Catalano, A. Carocci, G. Lentini, C. Franchini and D. Camerino, *Front. Pharmacol.*, 2012, **3**, 17.

61 J.-F. Desaphy, A. Dipalma, T. Costanza, C. Bruno, G. Lentini, C. Franchini, A. George and D. Conte Camerino, *Br. J. Pharmacol.*, 2010, **160**, 1521–1533.

62 D. Ragsdale, J. Mcphee, T. Scheuer and W. Catterall, *Proc. Natl. Acad. Sci. U. S. A.*, 1996, **93**, 9270–9275.

63 M. Vetta, L. González and J. Nogueira, *ChemistryOpen*, 2018, **7**, 475–483.

64 Q. Gong, H. Zhang, H. Zhang and C. Chen, *RSC Adv.*, 2019, **10**, 790–800.